minerals

MDPI

Article

Mineralogical and Chemical Specificity of Dusts Originating from Iron and Non-Ferrous Metallurgy in the Light of Their Magnetic Susceptibility

Mariola Jabłońska [1], Marzena Rachwał [2,*], Małgorzata Wawer [2], Mariola Kądziołka-Gaweł [3], Ewa Teper [1], Tomasz Krzykawski [1] and Danuta Smołka-Danielowska [1]

[1] University Laboratories of Atmospheric Survey, Faculty of Natural Sciences, Institute of Earth Sciences, University of Silesia, 60 Będzińska St., 41-200 Sosnowiec, Poland; mariola.jablonska@us.edu.pl (M.J.); ewa.teper@us.edu.pl (E.T.); tomasz.krzykawski@us.edu.pl (T.K.); danuta.smolka-danielowska@us.edu.pl (D.S.-D.)

[2] Institute of Environmental Engineering, Polish Academy of Sciences, 34 Skłodowska-Curie St., 41-819 Zabrze, Poland; malgorzata.wawer@ipis.zabrze.pl

[3] Institute of Physics, University of Silesia, 75 Pułku Piechoty 1a St., 41-500 Chorzów, Poland; mariola.kadziolka-gawel@us.edu.pl

* Correspondence: marzena.rachwal@ipis.zabrze.pl; Tel.: +48-322716481

Abstract: This study aims at detailed characteristics and comparison between dusts from various iron and non-ferrous metal production processes in order to identify individual mineral phases, chemical composition, and their influence on the values of magnetic susceptibility. Various analytical methods used include inductively coupled plasma optical emission spectroscopy, X-ray diffraction, scanning electron microscopy, and Mössbauer spectroscopy integrated with magnetic susceptibility measurements and thermomagnetic analysis. Metallurgical wastes that have arisen at different production stages of iron and non-ferrous steel are subjected to investigation. The analyzed dust samples from the iron and non-ferrous metallurgy differ in terms of magnetic susceptibility as well as their mineral and chemical composition. The research confirmed the presence of many very different mineral phases. In particular, interesting phases have been observed in non-ferrous dust, for example challacolloite, which was found for the first time in the dusts of non-ferrous metallurgy. Other characteristic minerals found in non-ferrous metallurgy dusts are zincite, anglesite, and lanarkite, while dusts of iron metallurgy contain mostly metallic iron and iron-bearing minerals (magnetite, hematite, franklinite, jacobsite, and wüstite), but also significant amounts of zincite and calcite.

Keywords: magnetic susceptibility; thermomagnetic curves; X-ray powder diffraction; scanning electron microscopy; Mössbauer spectroscopy; metallurgical dusts

Citation: Jabłońska, M.; Rachwał, M.; Wawer, M.; Kądziołka-Gaweł, M.; Teper, E.; Krzykawski, T.; Smołka-Danielowska, D. Mineralogical and Chemical Specificity of Dusts Originating from Iron and Non-Ferrous Metallurgy in the Light of Their Magnetic Susceptibility. *Minerals* **2021**, *11*, 216. https://doi.org/10.3390/min11020216

Academic Editor: Mark I. Pownceby

Received: 4 December 2020
Accepted: 17 February 2021
Published: 20 February 2021

1. Introduction

The region of Silesia, southern Poland, is a highly industrialized and urbanized area where active non-ferrous metal processing plants as well as steel- and iron-works are located. The plants are usually monitored, and they use highly efficient dust collectors so that the emission of pollutants into the air are not too harmful for the environment. However, these processes are not completely hermetic and dust particles, especially the finest ones are deposited on the Earth's surface, contaminating soils, ground water, plants, and finally incorporating into the food chain. The dusts emitted to the atmosphere by industry is nearly 17% of particulate matter in the Silesian Province and takes a second place in terms of the amount of anthropogenic pollution after dust from fossil fuel combustion [1]. Metallurgical processes are complex and heterogeneous, as are the substrates used in the production of metals and steel. Consequently, the products obtained at different stages of production and in various metallurgical processes are chemically and mineralogically diverse. Metallurgy, as well as another high-temperature technological processes

are the source of gaseous and dust emissions which also differ in their composition and properties. Dust formation depends on several conditions, such as temperature, oxygen availability, reduction-oxidation conditions, types of fuels, raw materials and additives used, as well as sampling position within the metallurgical plant. They are also specific to different technological processes that determine the properties of dusts containing technogenic magnetic particles (TMP) [2,3]. TMP have specific mineral and magnetic properties. Moreover, their well-developed specific surface area is characterized by an affinity for some elements [4,5]. TMP are mostly iron oxides with ferrimagnetic or antiferromagnetic properties, therefore their presence in dusts, soils and sediments can be easily detected by magnetic susceptibility measurements [6–8]. Iron-bearing minerals, and especially the most commonly occurred and used iron oxides, undergo numerous transitions during thermal processes, which constitute a large group of heterogeneous reactions leading to decomposition, alternate conversions, and the formation of various iron-bearing minerals, such as goethite, lepidocrocite, siderite, pyrite, pyrrhotite, vermiculite, ilmenite, and others [9,10]. Thermomagnetic analysis along with X-ray diffraction and Mössbauer spectroscopy are valuable methods for identification and the characterization of iron-bearing phases.

Therefore, many researchers have investigated microstructural and magnetic properties of dusts, especially fly ashes from power plants which use coal as a major source for energy generation [4,5,11–17]. Many publications have described the chemical composition and the content of basic elements of fly and bottom ashes [18–21]. The results of several publications on emissions from other industries such as refineries, cement, coke, or steel plants have been used to assess the critical issue of environmental pollution levels [22–26]. However, it is very important to determine the mineralogical phase composition of dusts, because very often the chemical composition alone is not sufficient to estimate whether individual types of dust are easily or sparingly soluble. Thus, this requires assessment of the ease with which TMP can penetrate the soil profile and living organisms. The mineralogy, magnetic susceptibility and size of the dust particles can help in modelling and assessing the impact of metallurgical dusts on the environment. The identification of the particular iron-bearing minerals formed during thermal transformations is a problem of scientific and technical importance. There are studies on dust emissions from iron and steel metallurgy or non-ferrous metal plants, but they were treated independently [27–31].

This study, therefore, aims at carrying out detailed characterization as well as comparing dusts from various iron and non-ferrous metal production processes in order to identify individual mineral phases, chemical composition, and their respective magnetic susceptibility. Various analytical methods (inductively coupled plasma optical emission spectroscopy, X-ray diffraction, scanning electron microscopy, and Mössbauer spectroscopy) integrated with magnetic susceptibility measurements and thermomagnetic analysis are used to better understand the chemical and mineralogical properties of metallurgical wastes generated at different production stages of iron and non-ferrous steel.

2. Materials and Methods

Twelve samples of dust from various technological processes used in metallurgical production of iron and non-ferrous metals were collected directly by qualified staff of four Polish plants (their names are protected by a confidentiality agreement). A total of eight samples were obtained from iron production sites employing various technological processes, including scale dust—sample No. 7, dust from de-dusting—sample No. 8, steelmaking dust—samples No. 16, 17, and 18; sinter dust—sample No. 20, and iron-bearing sludge dust—samples No. 22 and 23. Four dust samples from the production of non-ferrous metals were collected from various technological processes, such as sinter plant, zinc rectification, lead refinery, and shaft furnace.

2.1. Chemical Composition

Chemical composition was determined on the basis of the content of Cd, Cu, Cr, Fe, Mn, Pb, Zn, and V. The content of mentioned elements was analyzed using Inductively Cou-

pled Plasma Optical Emission Spectroscopy (ICP-OES; Avio 200 Perkin Elmer, PerkinElmer, Inc., Waltham, MA, USA) after mineralization in a mixture of nitric acid and hydrogen peroxide solution in a microwave oven.

2.2. Mineralogical Composition

Mineralogical composition and morphology of particles was analyzed using an environmental scanning electron microscopy (SEM) Philips XL 30 ESEM TMP, equipped with an analytical EDAX Sapphire type EDS (Energy Dispersive Spectroscopy) detector with ultra-thin window for analysis of the chemical composition of single dust particles (EDAX Corporate Headquarters EDAX, LLC, Mahwah, NJ, US).

Additionally, samples were investigated by X-ray powder diffraction (XRD) method using X'Pert PW 3710 and X'Pert Pro Model PW 3040/60 (PANalytical, Almelo, Holland) X-ray diffractometer. The analysis parameters were set to as follows: range: 2.5–65 or 5–90 °2Theta; time limit: 300 s; step size: 0.01 °2Theta. The weight fraction of minerals was estimated using the Rietveld Method module in the HighScore+ software (version 4.9) coupled with the ICSD 2015 and ICDD PDF 4+ 2018 database.

2.3. Iron-Bearing Phase Identification

Mössbauer spectroscopy method was applied in order to complete the characterization of the Fe-bearing minerals in the tested dusts, identify phases containing iron and determine the oxidation states of their Fe-ions. ^{57}Fe Mössbauer transmission spectra were recorded at room temperature with a POLON type Mössbauer spectrometer and a linear arrangement of a ^{57}Co:Rh source (15 mCi activity), a multichannel analyzer with 1024 channels (before folding), an absorber and a detector. A gas proportional counter LND–45431 was used as a gamma-ray detector. A 2-mm plastic filter was placed in the beam to absorb the 6 keV X-rays before they entered to the detector. The spectrometer was calibrated at room temperature with a 30 μm thick α-Fe foil. Numerical analysis of the Mössbauer spectra was performed by means of the WMOSS4 program ver. F (Ion Prisecaru, "WMOSS4 Mössbauer Spectral Analysis Software"). The mineralogical interpretations of the spectra was based on the Mössbauer Mineral Handbook [32]. The concentration of ferric and ferrous iron was determined from the spectral areas of the corresponding subspectra. Such analyses are complex issue due to their connection with the Mössbauer recoilless fraction [33–35]. It has been taken into account that the pulverized samples were mounted with the sample thickness of 7 mg/cm^2 in the holder. Such amount of the sample was optimal to reduce absorber thickness effects [36,37].

2.4. Magnetic Susceptibility

Mass-specific magnetic susceptibility and frequency dependent susceptibility using a dual frequency MS2B Bartington equipment (Bartington Instruments Ltd., Witney, UK) was measured. Dust samples (in the form of five subsamples of each kind of dust collected) after drying, weighting and placing in standardized Bartington 10 cc plastic vials were subjected to low field bulk magnetic susceptibility measurements (k) at low frequency [38]. Afterwards, the mass-specific (χ) magnetic susceptibility was calculated, taking into account a sample density (q), by the following equation: $\chi = k/q$ (m^3/kg). Additionally, thermomagnetic analysis using MFK1-FA Kappabridge device connected with CS4 High Temperature Furnace Apparatus (Agico Advanced Geoscience Instruments Co., Brno, Czech Republic) was performed to supplement mineralogical research. Measurements of the temperature variation of low-field magnetic susceptibility were carried out in the temperature range from ambient temperature to 700 °C (continuous heating and the following cooling) in an argon atmosphere. Thermomagnetic curves were measured in the 2 Am^{-1} to 700 Am^{-1} field and the operating frequency of 976 Hz. The "Cureval 8" program was used to process and visualize the obtained data [39].

3. Results and Discussion

Metallurgical processes, involving the extraction of metals from their ores and scrap, proceed in high temperatures (up to 2000 °C), which vary depending on the process (roasting, melting, sintering, casting, and rolling) [40]. The iron ores most often used for metallurgical purposes are deposits of iron oxides, mainly hematite and magnetite. On the other hand, in non-ferrous metallurgy the important minerals in zinc ores are sphalerite, zincite, franklinite, and smithsonite [41]. During these high temperature processes, minerals included in ores undergo numerous complicated transformation. As a result, iron or non-ferrous steel is produced, with a diverse chemical and mineral composition. Unfortunately, metallurgical processes also generate waste: dusts and slags of different composition and properties which are the subject of presented study.

3.1. Chemical Composition

Chemical analysis was performed to determine the content of cadmium, copper, chromium, iron, manganese, lead, zinc, and vanadium. These elements were selected in terms of additives that are used in the production of different types of steel and the production of non-ferrous metals that are used commercially. Chemical composition of dusts from various iron and non-ferrous metallurgy processes is presented in Table 1. The chemical composition of iron dust is fundamentally different from that of non-ferrous metal dust.

Table 1. Magnetic susceptibility and chemical composition of dust from different iron and non-ferrous metallurgical processes.

Kind of Process	Sample No.	χ	Cd	Cu	Cr	Fe	Mn	Pb	Zn	V
Iron Metallurgy										
		$\times 10^{-8}$ m^3/kg	mg/kg	mg/kg	mg/kg	%	%	%	%	mg/kg
scale	7	4633	0.25	1087	123	73.8	0.6	0	0	16.0
de-dusting dust	8	9488	570	1153	492	18.4	1.4	2.5	2.6	42.9
steel dust	16	1604	930	2477	1144	23.3	2.6	1.9	2.9	78.6
steel dust	17	9099	420	694	331	2.9	0.7	1.1	3.2	2.5
steel dust	18	5630	55	118	140	39.2	1.4	0.2	1.1	50.4
sinter dust	20	1950	10	105	49	48.6	0.1	0.1	0	18.2
iron-bearing sludge	22	5840	33	477	101	52.8	0.6	0.2	1.1	29.4
iron-bearing sludge	23	4994	8	269	185	63.0	0.6	0.2	0.9	74.8
Non-Ferrous Metallurgy										
		$\times 10^{-8}$ m^3/kg	%	mg/kg	mg/kg	%	mg/kg	%	%	mg/kg
zinc rectification	10	5	4.60	215	1	0	14	1.0	4.3	2.5
lead refinery	11	62	0.15	2484	7	0.2	3	3.3	3.2	2.5
sinter plant	9	440	2.80	4295	59	2.1	986	3.1	2.8	16.3
shaft furnace	12	873	0.47	1581	20	1.3	613	3.5	3.9	5.8

The content of cadmium in studied dusts is very diverse: from 0.25 mg/kg for scale from iron metallurgy to as much as 4.6%—for dust from the process of zinc rectification. A much higher content of this element in dusts from non-ferrous metallurgical processes is justified because of its content in Zn-Pb ores being a raw material. The results are comparable with Cd content (3.89%) in dust from a sintering machine of the zinc smelting plant obtained by Adamczyk and Nowińska [29] and in contrast to the dusts collected from electric arc furnaces, in which Cd content amounted only to 40 mg/kg [42]. Similarly, the content of zinc and lead is slightly higher for dusts from non-ferrous metallurgical processes.

In general, such elements as Fe, Mn, Cr, and V occur in much higher quantity in wastes from iron metallurgy. Only content of copper in dusts from both iron and non-

ferrous metallurgy varies in a wide range: from 105 mg/kg in sintering dust from the iron metallurgical processes up to 4295 mg/kg in sintering dust from non-ferrous metallurgy.

3.2. Mineral Composition

Mineral composition of dusts determined using the X-ray powder diffraction method (XRD) is presented in Tables 2 and 3. Performed analysis of single particles of industrial dust using the SEM coupled with the EDS spectrometer allowed the observation of particle morphology together with the determination of chemical composition of individual dust particles, which confirmed the presence of mineral phases obtained using the XRD analysis.

Table 2. Mineral composition of dust from iron smelting processes on the basis of XRD analyses by the Rietveld method in wt%.

Component	Formula	Scale	De-Dusting dust	Steel Dust			Sinter Dust	Iron-Bearing Sludge	
Sample number:		7	8	16	17	18	20	22	23
franklinite-jacobsite	$(Zn,Mn^{2+},Fe^{2+})(Fe^{3+},Mn^{3+})_2O_4$		30.0	44.5	52.5				
magnetite	Fe_3O_4	48.0	24.5	27.0		30.0	37.5	9.5	9.0
hematite	Fe_2O_3	8.5				46.5	34.0	23.0	
wüstite	FeO	43.5						30.0	39.5
quartz	SiO_2		3.0	1.5			9.5		
zincite	ZnO		38.5	24.0	40.5	2.5			
laurionite	PbClOH		1.5	1.5	1.5				
sylvine	KCl		2.5	1.5	1.5		7.5		
halite	NaCl				4.0		3.0		
calcite	$CaCO_3$					4.5	8.5	23.0	30.0
portlandite	$Ca(OH)_2$					4.0			
graphite	C					12.5			
srebrodolskite	$Ca_2(Fe^{3+})_2O_5$							1.5	2.0
iron	Fe							13.0	19.5
sum		100	100	100	100	100	100	100	100

Table 3. Mineral composition of dust from non-ferrous metallurgy based on XRD analyses by Rietveld's method in wt%.

Component	Formula	Process and Sample Number			
		Zinc Rectification	Lead Refinery	Sinter Plant	Shaft Furnace
		10	11	9	12
zincite	ZnO	95.0	28.0	2.5	66.0
gordaite	$NaZn_4SO_4Cl(OH)_6 \times 6H_2O$			11.5	2.0
challacolloite	KPb_2Cl_5			45.0	
palmierite	$K_2Pb(SO_4)_2$		0.5	3.5	12.5
anglesite	$PbSO_4$		36.0	17.5	13.5
matlockite	PbClF			13.5	1.0
lanarkite	Pb_2OSO_4		34.0	2.0	2.0
osakaite	$Zn_4SO_4(OH)_6 \times 5H_2O$			2.0	1.5
lahnsteinite	$Zn_4SO_4(OH)_6 \times 3H2O$				1.5
sylvine	KCl		1.5		
galena	PbS			2.5	
otavite	$CdCO_3$	2.0			
monteponite	CdO	3.0			
sum		100	100	100	100

A significantly different mineral composition was observed in the dusts obtained from processes of iron and non-ferrous metallurgy. Dusts from the iron metallurgy processes are characterized by a significantly different mineral composition. They are dominated by iron oxide phases from wüstite FeO through hematite Fe_2O_3 to various types of spinels,

such as magnetite Fe_3O_4, or franklinite–jacobsite (Zn, Mn^{2+}, Fe^{2+})(Fe^{3+}, Mn^{3+})$_2O_4$. The composition of iron dust varies depending on the process. The following 15 phases were determined in total: franklinite–jacobsite (Zn, Mn^{2+}, Fe^{2+})(Fe^{3+}, Mn^{3+})$_2O_4$, magnetite Fe_3O_4, hematite Fe_2O_3, wüstite FeO, quartz SiO_2, zincite ZnO, laurionite PbClOH, sylvine KCl, halite NaCl, calcite $CaCO_3$, portlandite $Ca(OH)_2$, graphite C, srebrodolskite $Ca_2(Fe^{3+})_2O_5$, periclase MgO, and metallic Fe.

The scale dust was characterized by the presence of only three oxide phases: magnetite—approx. 48% (Figures 1 and 2), wüstite—43.5% and hematite—8.5% (Figure 2). The scale dust sample was characterized by relatively large, massive particles, the size of which usually exceeded 15 µm. The dominant element in these dusts was iron present in two Fe-oxidation states or phases, Fe^{2+} and Fe^{3+}.

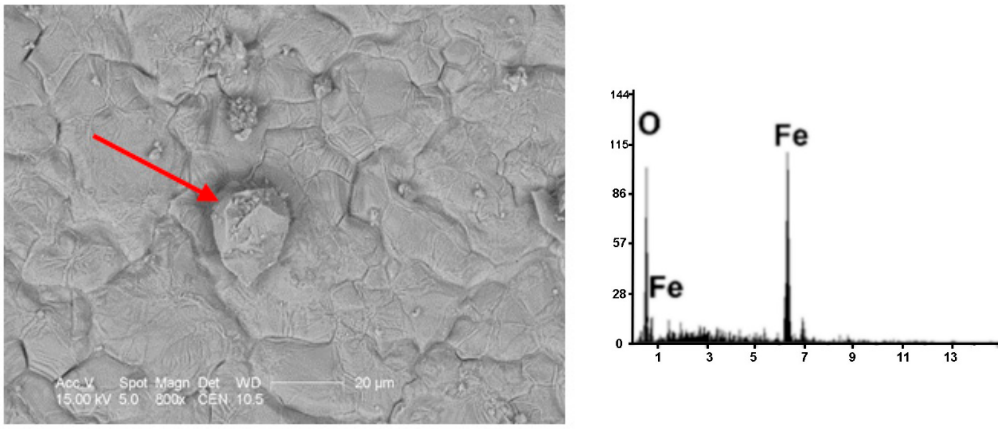

(**a**) (**b**)

Figure 1. Scale dust (No. 7): (**a**) Scanning electron microscopy (SEM) image of the magnetite crystal (indicated with red arrow); (**b**) the EDS spectrum.

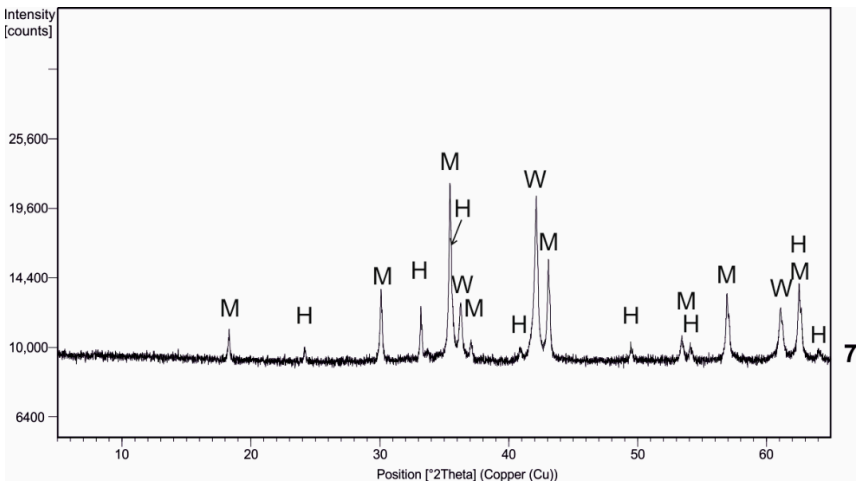

Figure 2. X-ray powder diffraction (XRD) pattern of sample No. 7 (scale). Symbol explanation: M—magnetite, H—hematite, W—wüstite.

The dominant components in dust from de-dusting were spinels, which in total constituted approx. 54.5% (Table 2). Further, zincite was a frequently occurring component of these dusts, the amount of which was estimated at nearly 38.5%. The other components were quartz 3%, sylvine 2.5% and laurionite 1.5% (Figures 3 and 4). Laurionite particles occur as elongated forms, the length of which ranges from 1.5 to 12 µm and a width up to 2.5 µm (Figure 3).

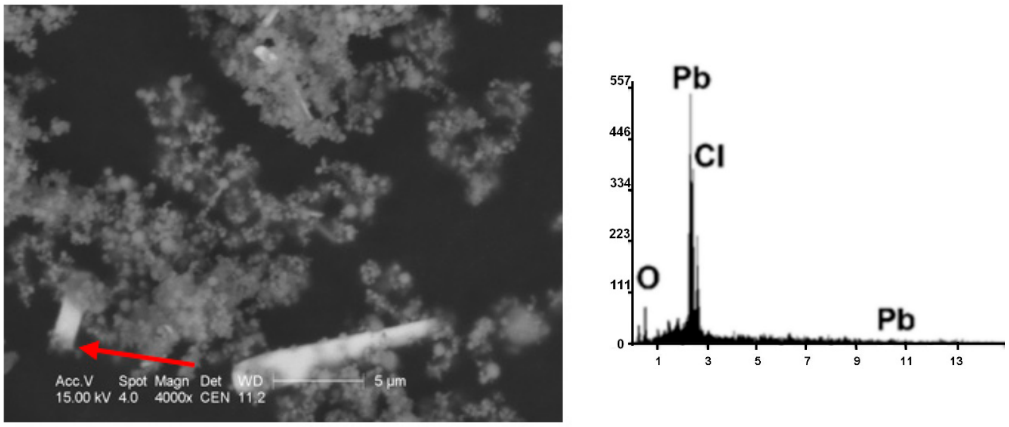

(**a**) (**b**)

Figure 3. Laurionite particle in dust from de-dusting, sample No. 8: (**a**) SEM image (laurionite is indicated by a red arrow); (**b**) the EDS spectrum.

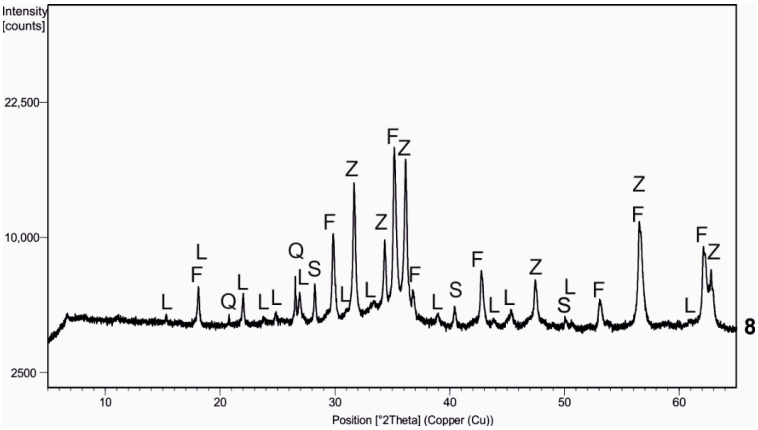

Figure 4. XRD pattern of de-dusting dust (sample No. 8). Symbol explanation: F—franklinite–jacobsite, L—laurionite, Q—quartz, S—sylvine, Z—zincite, M—magnetite.

Zincite particles in de-dusting and steel dust were present in the form of aggregates consisting of small oval forms. Their amount ranged from 2.5 to 40.5%. Zincite was not observed in sinter dust and iron-bearing sludge. It is obvious that particles containing iron oxides, mainly spinels like franklinite–jacobsite and magnetite, dominated in the steel dust (Figure 5). The content of franklinite–jacobsite reached the maximum value of 52.5%. The magnetite content was in the range from 9% in iron-bearing sludge dust up to 48% in the scale.

Hematite was also a common Fe oxide. Its content, depending on the process, ranged from 8.5% in scale up to 46.5% in steel dust (Table 2). Iron oxide in the form of wüstite were also present in the dust from the iron metallurgy, but this phase was observed only in the scale (43.5%) and in iron-bearing dust (30–39.5%).

The sintering dust is characterized by the content of six minerals (Table 2). The most abundant particles consists of iron oxides (magnetite and hematite), whose share reaches the value of 71.5%. Apart from iron oxides, the presence of quartz and calcite in amounts not exceeding 10% each is determined. Moreover, in the sintering dust, chlorides such as sylvine and halite are present in very small amounts (10.5%) and can result from the formation of secondary dust during the production process. In particular, this applies to dusts from steel production where coal (coke) is used for their production. In various coal combustion processes, HCl is emitted, which may react with other components, forming NaCl or KCl. In addition, in a lead refining process, baths are made in various solutions (e.g., potassium hydroxide or hydrochloric acid).

Among all types of dust from iron metallurgical processes, the iron-bearing sludge dust (Figure 6) contains the lowest amount of magnetite (not exceeding 10%) and a high content of wüstite (30–40%), as well as metallic iron particles ranged from 13 to 19.5%. These particles are characterized by sharp-edged shapes, and their size usually exceeds 10 µm (Figure 7).

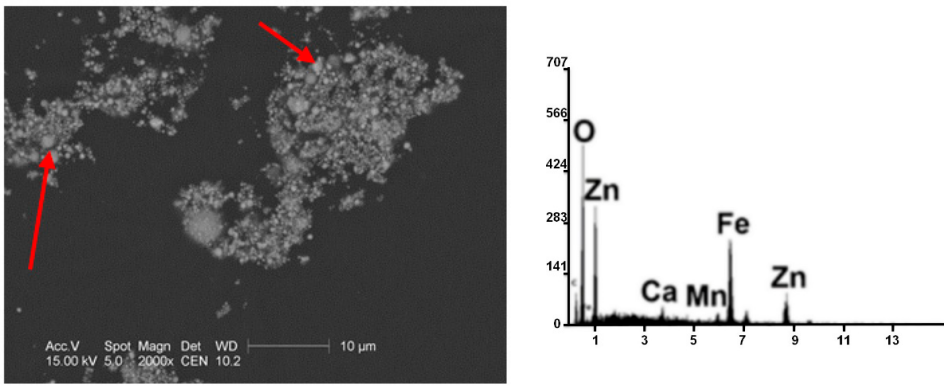

(**a**) (**b**)

Figure 5. Particles composed of franklinite–jacobsite in steel dust, sample No. 17: (**a**) SEM image of franklinite–jacobsite particles (indicated with red arrows); (**b**) the EDS spectrum.

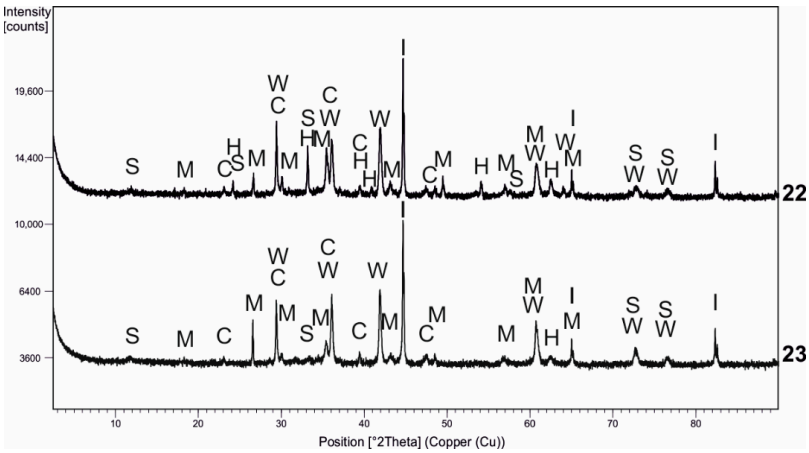

Figure 6. XRD pattern of sample No. 22 and 23. Symbol explanation: C—calcite, H—hematite, I—iron, M—magnetite, S—srebrodolskite.

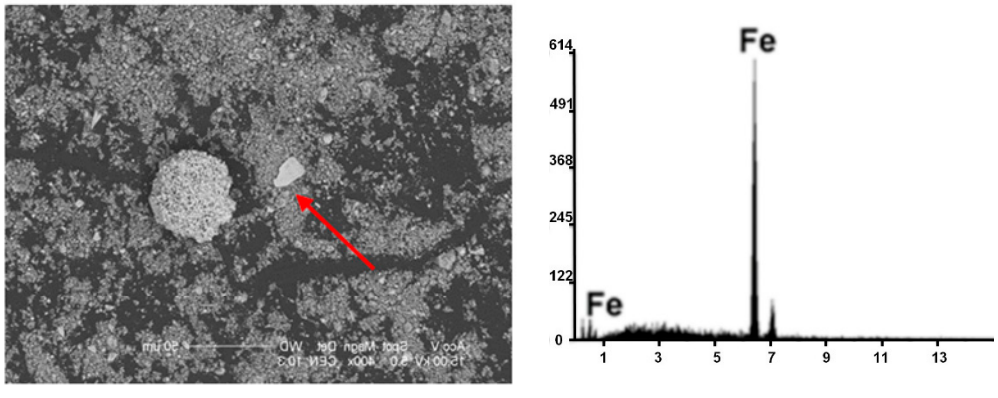

(**a**) (**b**)

Figure 7. Metallic iron particle (indicated with red arrow) in iron-bearing sludge dust (sample No. 22): (**a**) SEM image; (**b**) the EDS spectrum.

The chemical analysis of the metallurgical dusts revealed large diversity: some elements are present in significant amounts (percentages) and elements with only trace content. Sample No. 16 (steel dust) is characterized by the lowest magnetic susceptibility and the highest content of majority of elements, such as Mn, Cr, Cu, Cd, and V. Unfortunately, any mineral phases with Mn, Cr, or Cu have not been identified in this sample. The possible reasons for this could be the following:

(i) amount of phases containing these elements in the sample was under detecting limit of the XRD method;

(ii) Mn and Cr can be present in ferritic form whose peaks can be covered by the peaks of magnetite and franklinite (coincidence of peaks);

(iii) they can be present in the spinel phase lattice of franklinite and magnetite and not as separate phases [43].

The composition of dust from non-ferrous metallurgy varies depending on the process. A total of 13 phases have been identified: palmierite $K_2Pb(SO_4)_2$, anglesite $PbSO_4$, osakaite $Zn_4SO_4(OH)_6 \times 5H_2O$, gordaite $NaZn_4SO_4Cl(OH)_6 \times 6H_2O$, matlockite PbClF, galena PbS, zincite ZnO, sylvine KCl, challacolloite KPb_2Cl_5, otavite $CdCO_3$, monteponite CdO, lanarkite Pb_2SO_5, and lahnsteinite $Zn_4SO_4(OH)_6 \times 3H_2O$.

The most abundant component in the dust from non-ferrous metallurgy is zincite (Table 3, Figure 8a,b and Figure 9), the highest content of which was 95% found in the dust from the zinc rectification process and 66% in the dust from the shaft furnace. In the dust from lead refineries, zincite occupies 28% and it is the third most abundant component after the 36% of anglesite and 34% of lanarkite. Zincite occurs in the form of hexagonal bars, often ending in a pyramidal shape, and it also forms twins. The sizes of individual zincite crystals range from 1.5 to 8 μm, and larger sizes over 5 μm are formed by zincite aggregates (Figure 8a,b).

Only three phases dominate in the zinc rectification process: Zn oxide in the form of zincite and cadmium oxide in the form of monteponite and cadmium carbonate in otavite (Figure 9). Individual particles consisting of cadmium oxides had a size below 2 μm with irregular shapes, often forming aggregates larger than 4 μm with spherical forms (Figure 10).

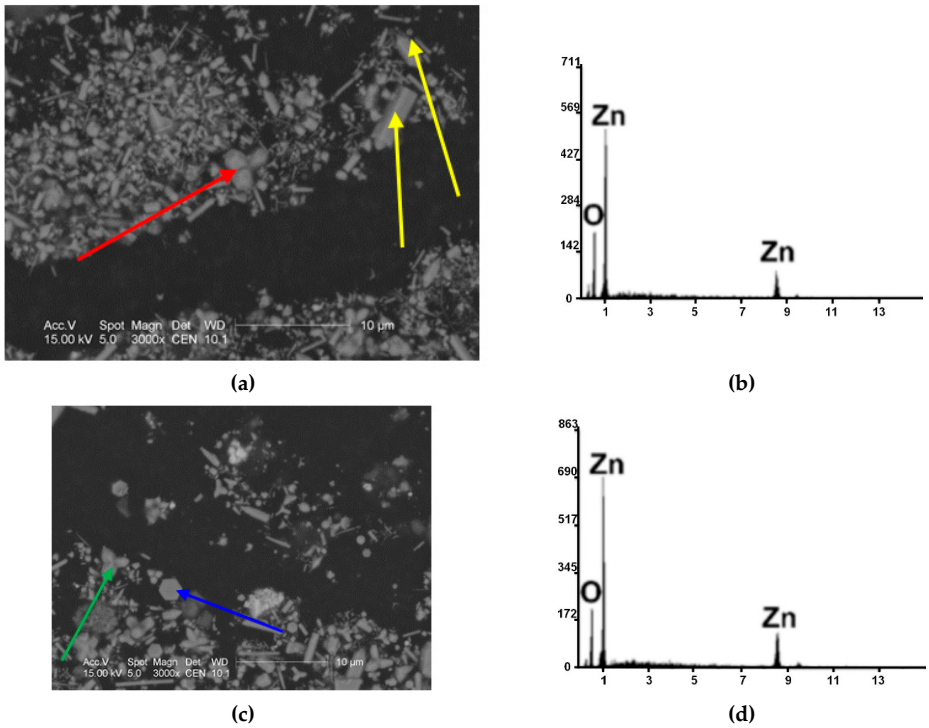

Figure 8. Dust from the Zn rectification process (sample No. 10): (**a**,**c**) SEM images: red arrow indicates zincite crystals forming twins; yellow arrows—single zincite crystals in the form of a column, sometimes with pyramidal ends; green arrow—twinning of columnar zincite crystals with pyramidal ends; blue arrow—hexagonal crystal of zincite; (**b**,**d**) the EDS spectrum.

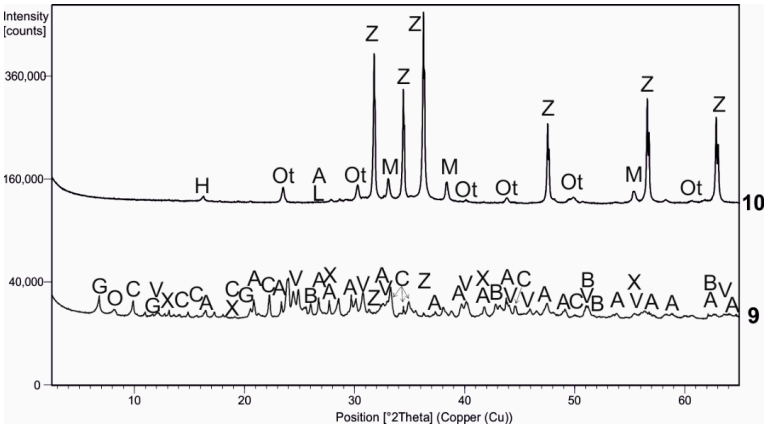

Figure 9. XRD pattern of sample No. 10 (Zn rectification) and No. 9 (sinter plant). Symbol explanation: A—anglesite, B—galena, C—challacolloite, G—gordaite, M—monteponite, O—osakaite, Ot—otavite, V—matlockite, X—palmierite, Z—zincite.

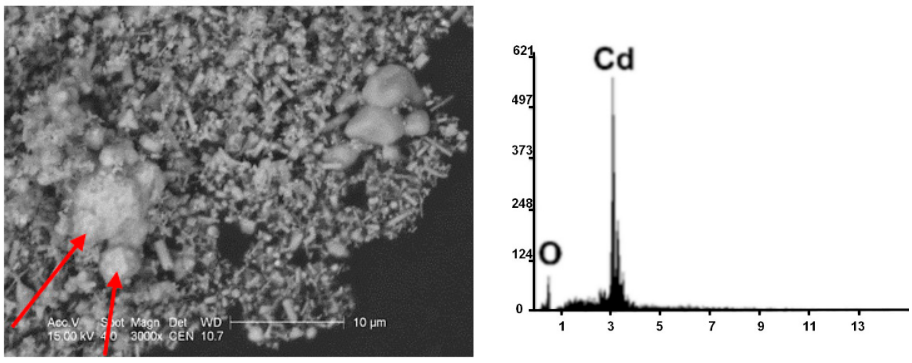

(**a**) (**b**)

Figure 10. Particles from the zinc rectification process: (**a**) SEM image; the red arrows indicate components with the composition of cadmium oxides, probably monteponite CdO; (**b**) the XRD spectrum.

Moreover, in the lead refinery process, only five phases were distinguished: anglesite, lanarkite, zincite, sylvine and palmierite (Table 3). The first three minerals account for nearly 98% of all components in the described non-ferrous metallurgical process.

The lead sulphates observed using SEM exist as the two phases of an anglesite and lanarkite (Figure 11). The lead sulphate particles appear in spherical forms and their sizes do not exceed 2–3 µm (Figure 11).

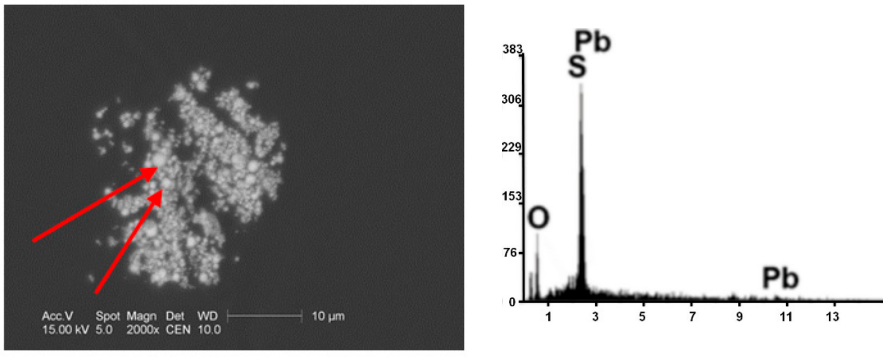

(**a**) (**b**)

Figure 11. Dust particles from the lead refinery process (sample No. 11): (**a**) SEM images; the red arrows indicate lead sulphate: anglesite $PbSO_4$ and lanarkite; (**b**) the EDS spectrum.

The dust from the sinter plant was characterized by the greatest variety of minerals (Figure 9). Nine different mineral phases have been identified. The dominant component of approx. 65% of all particles are challacolloite KPb_2Cl_5 (Figure 12 and Table 3).

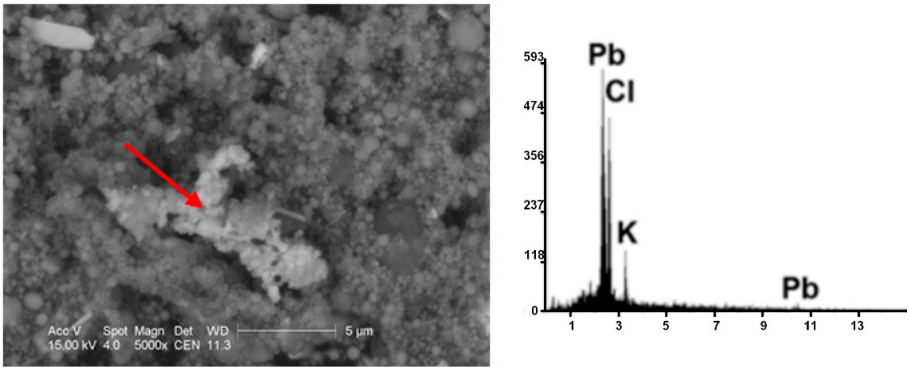

(**a**) (**b**)

Figure 12. Dust particles from the sinter plant (sample No. 9): (**a**) SEM image; red arrow indicates a challacolloite KPb_2Cl_5 aggregate; (**b**) the EDS spectrum.

The sizes of single particles with the challacolloite composition do not exceed 1 µm. Most often they form aggregates made of small oval particles (Figure 13).

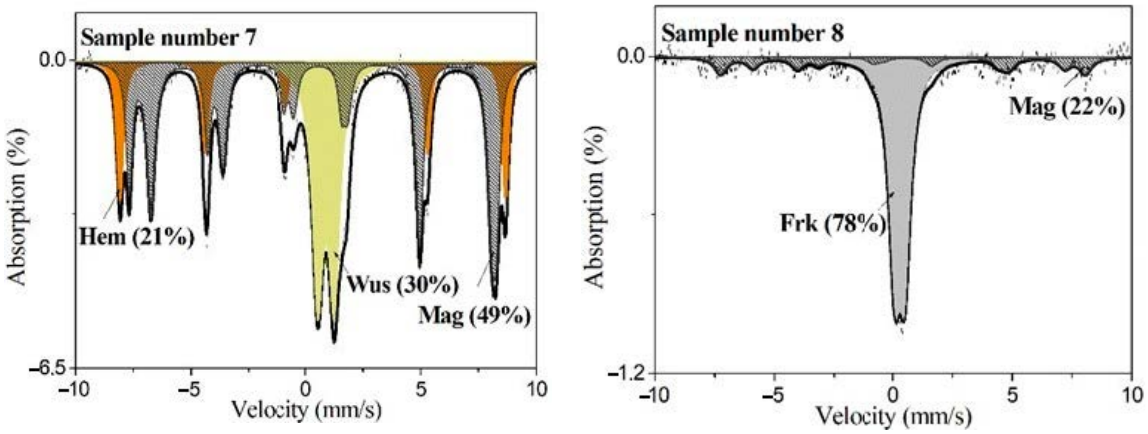

Figure 13. Mössbauer spectra obtained for scale (No. 7) and dedusting dust (No. 8). Fitted subspectra, their assignments and contribution are visible on the spectra; Hem—hematite, Mag—magnetite, Wus—wüstite, Frk—franklinite. Absolute errors are estimated at ± 1% for components areas.

In dust collected from the shaft furnace, eight mineral phases were distinguished. Zincite had the largest share, about 66% (Table 3). Other components present in the amount of 28% are lead sulphates (anglesite, palmierite, and lanarkite). Among the dust from the shaft furnace, osakaite and lahnsteinite were identified in the amount of 1.5 each. The rare matlockite PbClF in the amount of approximately 1% was also found (Table 3).

3.3. Iron-Bearing Phase Identification

To obtain more local information, Mössbauer spectroscopy of iron has become an established method in investigation of minerals. This method gives information about oxidation states and coordination numbers, which are identified on the basis of the magnitudes of the isomer shifts (IS) and quadrupole splitting (QS). The isomer shift is extremely sensitive to the oxidation state of the sample. IS values predictably decrease with increasing s-electron density around the nucleus, so they depend not only on oxidation state but also on the type and bond lengths of ligands coordinated to the Fe atoms. The upper

limit of isomer shift value for Fe^{3+} in tetrahedral coordination is approximately 0.25 mm/s, whereas the lower limit for octahedral Fe^{3+} is approximately 0.29 mm/s. For Fe^{2+}, values of IS > 1.20 mm/s are generally attributed to eightfold or dodecahedral coordination, values of 1.20 > IS > 1.05 mm/s are generally octahedral, and values of 1.05 > IS > 0.90 mm/s are assigned to tetrahedral occupancy [44]. The quadrupole splitting is a consequence of the quadrupole interaction (a measurable parameter of it). It is due to the asymmetry of the electron density distribution around the nucleus. In general, QS for Fe^{2+} >> QS for Fe^{3+}. Furthermore (as a general rule), the larger the QS, the more distorted the coordination polyhedron surrounding the Fe atom [44].

The measured Mössbauer spectra together with fitted components and their assignment obtained for investigated samples of technogenic dusts are presented in Figures 13–15, Table 4, and Table S1 in Supplementary Materials. By using ^{57}Fe Mössbauer spectroscopy, different iron compounds present in a solid mixture can be identified. The relative concentrations of iron-bearing phases (Table 4) can be estimated by spectra fitting. The samples have paramagnetic as well as magnetic fractions. All spectra are dominated by Fe^{3+} phases, accounting for 70–100% of the total iron (except for samples of iron-bearing sludge).

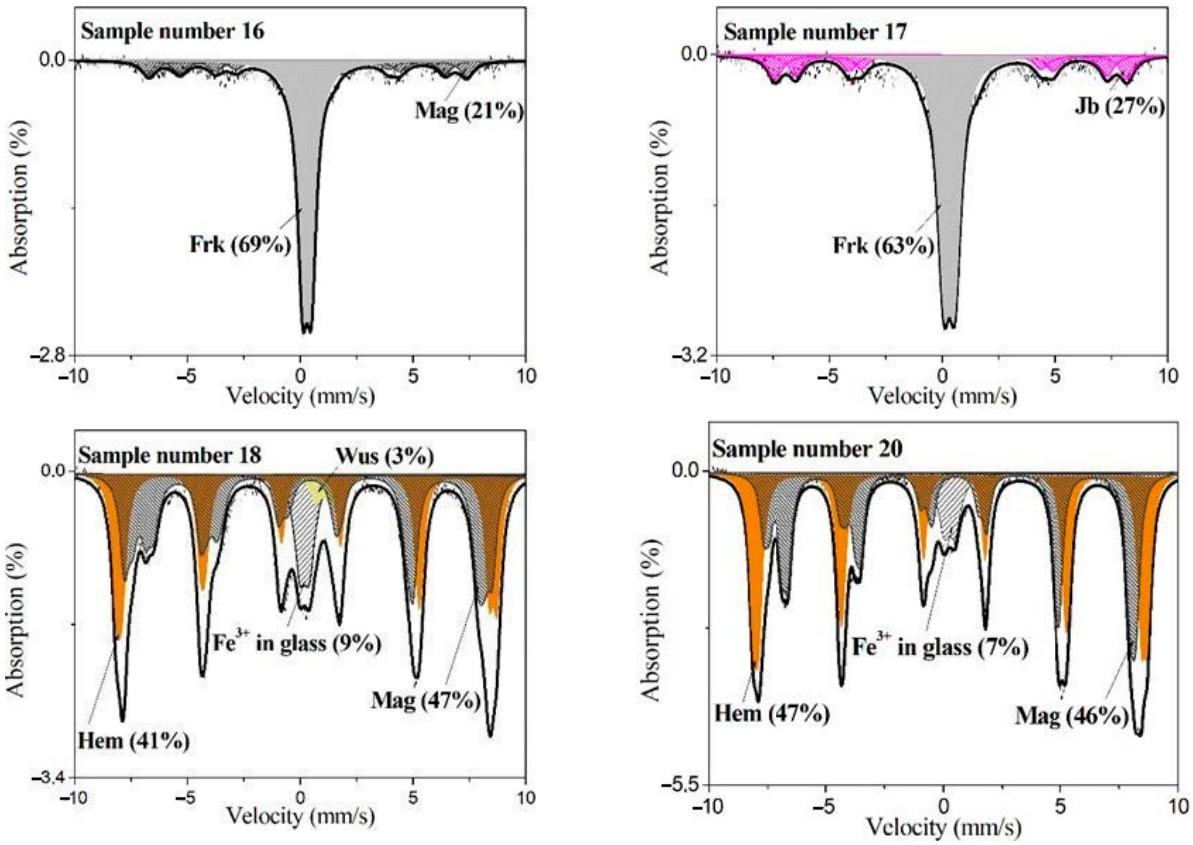

Figure 14. Mössbauer spectra obtained for steel dusts (No. 16, 17, and 18) and sinter dust (No. 20). Fitted subspectra, their assignments and contribution are visible on the spectra; Frk—franklinite, Hem—hematite, Mag—magnetite, Wus—wüstite, Jb—jacobsite. Absolute errors are estimated at ± 1% for components areas.

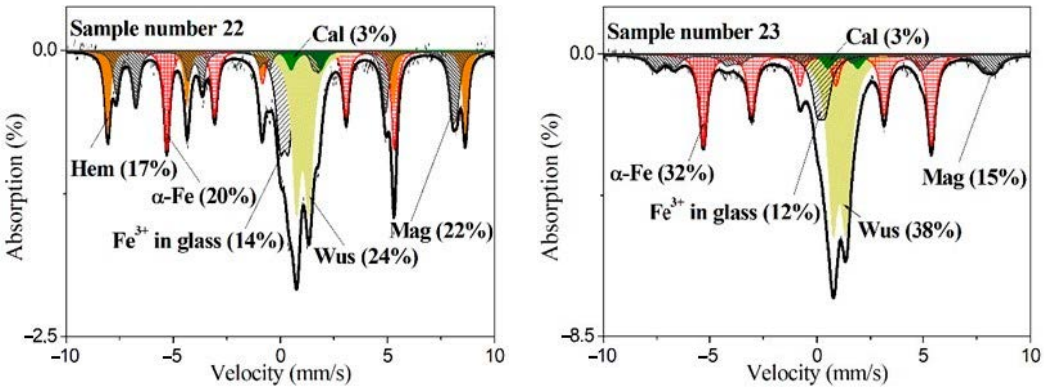

Figure 15. Mössbauer spectra obtained for iron-bearing sludges (No. 22, 23). Fitted subspectra, their assignments and contributions are visible on the spectra; Hem—hematite, Mag—magnetite, Wus—wüstite, Cal—calcite.

Table 4. Fe-bearing phases concentration (in % with an error ± 1%) of dust from iron smelting processes on the basis of Mössbauer spectroscopy analyses.

		Component							
Kind of Dust	**Sample No.**	**Jacobsite**	**Franklinite**	**Magnetite**	**Hematite**	**Wüstite**	**Fe^{2+} in Calcite**	**Fe^{3+} in Glass**	**Iron**
scale	7			49	21	30			
de-dusting dust	8		78	22					
steel dust	16		86	14					
	17	20	80						
	18			47	41	3		9	
sinter dust	20			46	47			7	
iron-bearing sludge	22			22	17	24	3	14	20
	23			15		38	3	12	32

Mössbauer spectra of the scale dust was fitted with three sextets and one quadrupole doublet (Figure 13). Two of the sextets were fitted using hyperfine magnetic fields (B_{hf}) 49.7 and 46.2 T, quadrupole splitting (QS) zero for both, isomer shift (IS) 0.35 and 0.68 mm/s, respectively, and are attributed to an inverse spinel magnetite phase Fe_3O_4. The remaining sextet fitted with parameters Bhf =52.1 T, QS = 0.16 mm/s and IS = 0.37 mm/s was attributed to hematite Fe_2O_3; however the positive quadrupole shift of hematite indicates impurities. The Mössbauer parameter values are IS = 0.90 mm/s and QS = 0.70 mm/s, which correspond to the presence of wüstite ($Fe^{2+}O$). Mössbauer spectra obtained for dust from dedusting (No. 8) and two steelmaking dust (No. 16, 17) look very similar (Figures 13 and 14). Iron appears only as ferric state. The dominating fraction (62–78%) is the paramagnetic doublet. Its hyperfine parameters, IS = 0.31 mm/s and QS from 0.39 to 0.43 mm/s, indicated franklinite. In the remaining parts of the spectra, iron appears in the magnetite (sample No. 8 and 16) and in jacobsite (sample No. 17).

The main Fe-containing phases in the sample No. 18 (steelmaking dust determined from spectra absorption areas) are hematite (41%) and magnetite (47%) (Figure 14 and Table 4). Furthermore, two doublets were also observed: the first with IS = 1.03 mm/s and QS = 0.63 mm/s correspond to the presence of Fe^{2+} in wüstite, while the second doublet with IS of about 0.19 mm/s and QS = 0.42 mm/s, is assigned to Fe^{3+} ions. It might be assumed that this doublet corresponds to iron-containing glass [45,46]. Hematite and magnetite are main magnetic Fe-bearing phases present in the sinter dust sample (Figure 14; Table 4). The observed Mössbauer parameter values for the spectrum of the ferric iron doublet of this sample can be interpreted to be iron-containing glass [45,46]. Mössbauer spectra of the iron-bearing sludge dusts, samples No. 22 and 23, contain the highest amount of wüstite, from 24 to 38%, respectively (Figure 15). This phase is represented on the spectrum by

paramagnetic doublet with hyperfine parameters IS = 1.05 mm/s and QS = 0.61 mm/s. Paramagnetic part of Fe-bearing phases in these samples form also another doublet, which parameters indicate Fe^{3+} in amorphous matrix. Sextet, with B_{hf} = 33T, connected with metallic iron was also detected on Mössbauer spectra of the iron-bearing sludge dusts. Its concentration amounts to 20% and 32% for samples No. 22 and No. 23, respectively. The remaining part of these spectra constitute iron oxides, which are hematite and magnetite in sample No. 22 and only magnetite in sample No. 23.

In general, the Mössbauer spectroscopy study is consistent with the results of XRD method. However, it is pertinent to bear in mind that there could be minor contribution of some minerals below detection limit (1%) in samples analyzed by the XRD method.

3.4. Magnetic Susceptibility

Magnetic susceptibility depends on the geochemical and mineralogical composition of investigated material, and in particular on the abundance of iron-bearing magnetic minerals. Dusts originated from the iron metallurgy are characterized by mass-specific magnetic susceptibility (χ) ranged from 1604 (steel dust) to 9488 $\times 10^{-8}$ m^3/kg (de-dusting system generated in the process of iron steel production). There are three samples of steelmaking dusts collected at various stages of electrostatic precipitators with very diverse values of χ: 1604, 5630 and 9099 $\times 10^{-8}$ m^3/kg. The reason for this is the fact that the dust came from different mills, which rely on their own steel production technologies and are based on different compositions of the furnace charge of pig iron and additives used in the production process (Table 1). Surprisingly, when comparing these three samples of steel dust whose magnetic susceptibility ranges from 1064 to 9099 $\times 10^{-8}$ m^3/kg, it appears that the most magnetic mineral fractions (magnetite and hematite) were identified in the sample with susceptibility equal to 5630 $\times 10^{-8}$ m^3/kg. Sample No. 18 with the highest χ contains jacobsite and franklinite. This situation can be explained by the method of measurements and analyses. Measurements of magnetic susceptibility are performed on a relatively large sample (approximately 10 g), while mineralogical and Mössbauer spectroscopy analyses—on a sample approximately 100 times smaller, so there is a possibility of encountering single, highly magnetic grains in the sample, which does not exhibit the highest magnetic susceptibility value.

Dusts from non-ferrous metallurgy reveal much lower mass-specific magnetic susceptibility values ranged from 5 to 873 $\times 10^{-8}$ m^3/kg for dust samples from the zinc rectification process and shaft furnace, respectively (Table 1). Values of χ obtained for dusts collected from iron metallurgy installation can be compared to those emitted by hard coal combustion exhibiting χ in range of 1485–8516 $\times 10^{-8} m^3/kg$, while χ values of dusts from non-ferrous metallurgy are in comparable ranges as χ values for lignite and cement dust [4,5]. Such a wide range of magnetic susceptibility is indicative of complex and variable mineral composition of TMP contained in dusts.

Thermomagnetic (k-T) curves of investigated samples are plotted in Figure 16, curves No. 7, 8, 16–18, 20, 22, and 23 represent dusts from iron metallurgy, while charts No. 10, 11, 9, and 12—dusts from non-ferrous plant. Differences in the thermomagnetic curve runs indicate varied composition of magnetic minerals. The k-T curves of iron metallurgy dusts are distinct from those of non-ferrous dusts mainly by a range of magnetic susceptibility which for the former reaches the values of several thousand, and for the latter—only a few dozen (max. 300) $\times$ 10^{-5} SI units. However, the thermomagnetic behavior for all samples shows a Curie temperature (T_C) at about 570–590 °C, indicating the presence of magnetite as the dominant magnetic carrier. The k-T curve of the scale sample (No. 7) differs from the others by the Hopkinson-like peak which characterizes the ferromagnetic to super-paramagnetic transition of the amorphous phase [6]. Magnetic susceptibility slowly increases with temperature and passes through a maximum followed by a sharp fall at the Curie temperature of magnetite. Temperature magnetic susceptibility dependence of sinter dust (No. 20) exhibits similar course, but the Hopkinson peak is much wider. The k-T curve of de-dusting dust (No. 8) looks completely different. A sharp decline in k from room

temperature to T_C of ~580 °C characteristic of magnetite, with a hump at ~370 to 400 °C followed by the larger drop in k. This can be related to the presence of franklinite which was found on the basis of the earlier discussed X-ray patterns and Mössbauer spectra. The k-T curves for samples No. 16, 17, and 9 have similar courses, however they exhibit different behavior after reaching temperature of 580–600 °C. On the heating curves of steel dust and dust after zinc rectification a continuous drop in k up to 700 °C is observed suggesting the presence of high-temperature magnetic phase, like metallic iron, which exhibits a T_C of 780 °C [8,47,48] or a significant amount of hematite (the Neel temperature of 675 °C) [49]. Four samples (No. 7, 18, 20, and 12) are characterized by cooling curves above heating ones indicating thermally induced neoformation of magnetite. The cooling and heating curves are irreversible, what means that magnetic minerals present in dust samples are not stable and undergo thermo-transformations during heating, e.g., transformation of maghemite to hematite between 300 and 450 °C [50].

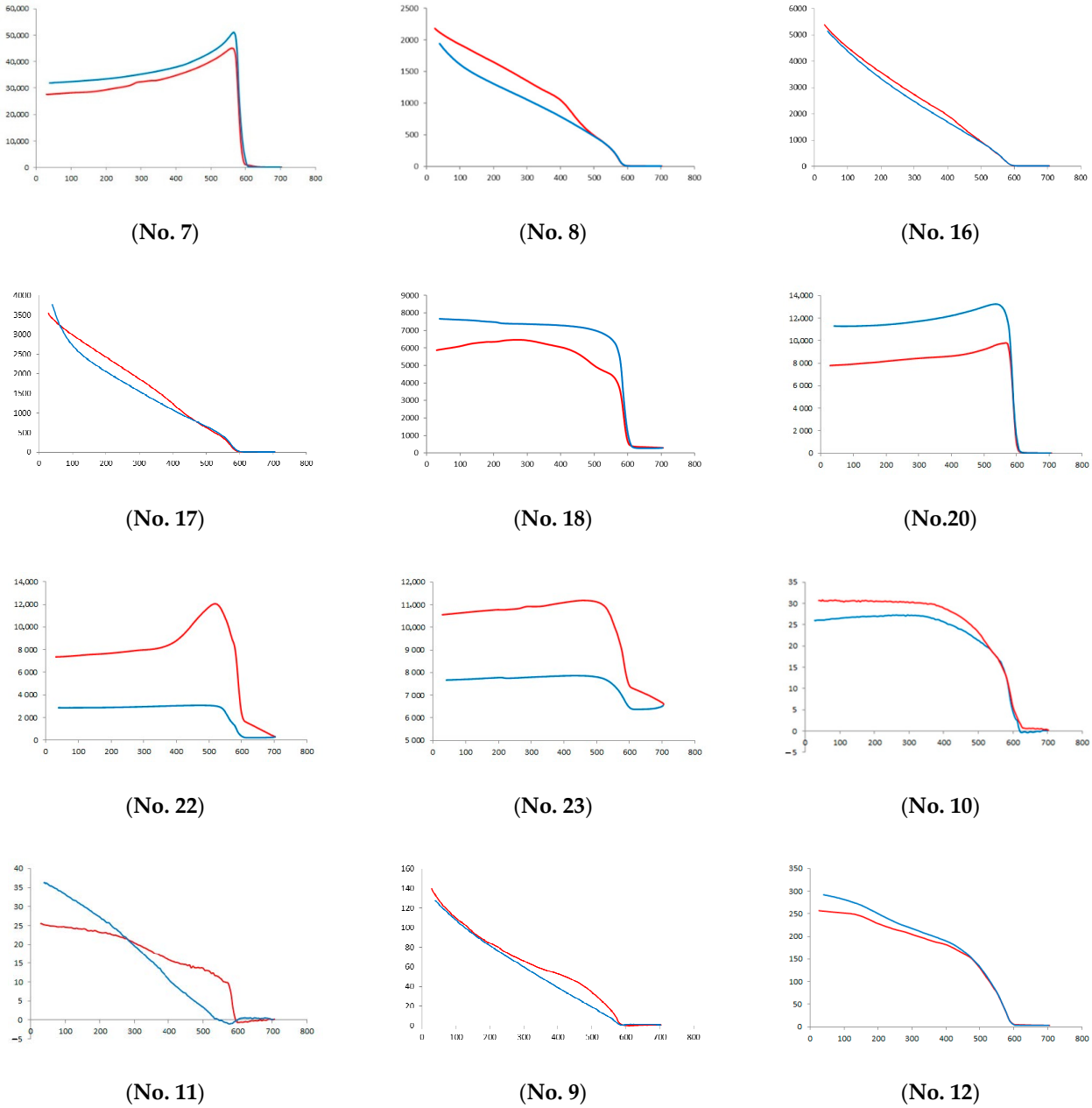

Figure 16. The k-T curves (k (×10-5 SI units) is presented on the Y-axis and T (°C)—on the X-axis) of investigated dust samples. The heating lines are in red and cooling lines—in blue.

4. Conclusions

The analyzed dust samples from the iron and non-ferrous metallurgy are characterized by different chemical and mineral composition, as well as magnetic susceptibility values.

The analyses carried out with the use of SEM, XRD, and Mössbauer spectroscopy clearly showed a very high content of magnetite, franklinite and jacobsite in dusts from iron metallurgy processes, the content of which is at a level exceeding 50% of all components contained in these dusts. These results are in agreement with chemical composition of dust samples which contain up to 74% of iron. The results show that particles of metallic iron are observed only in dusts originating from the iron-bearing sludge. These particles often have sharp-edged shapes, although their spherical forms are also encountered [1]. Dusts from iron metallurgy processes, containing iron oxides in the form of magnetite or franklinite–jacobsite differ in morphology from other particles of similar composition, which were found in dusts from coal combustion in power plants. In iron metallurgy these dusts are usually sharp-edged, massive particles with sizes exceeding 4 μm, while dusts from fossil fuel combustion are characterized by spherical forms, the size of which can be from 1–2 μm to even 50–60 μm [4,51]. What is more, in metallurgical dusts any spherical Fe-bearing aluminosilicate glassy particles were not detected, while abundance of spheroidal aluminosilicates has been considered as Anthropocene index characteristic for fossil fuel combustion [52].

Fe-poor dusts from non-ferrous metallurgy, with practically no minerals in the form of Fe oxides, showed the lowest magnetic susceptibility. Characterization of the mineral composition confirmed the presence of zinc, lead and cadmium-containing minerals. Similarly, the results of the analysis of the chemical composition of the dusts indicated that the highest levels were found for such heavy metals as: zinc, lead, and cadmium. Their total amount in the analyzed dusts amounted to nearly 10%.

The dust from the non-ferrous metallurgy was characterized by particle sizes usually below 10 microns. Such a fine fraction of dusts containing heavy metals, considered as toxic, after entering the atmosphere, can stay in it for a long period of time, which affects their distant movement from the emission source and causes environmental pollution [1,53].

The non-ferrous metallurgy dusts are constituted by lead chlorides and lead sulphates, such as challacolloite, palmierite, and matlockite, the amount of which in the analyzed samples ranged from 0.5% to 45%. Another characteristic minerals found in these dusts are zincite, anglesite, and lanarkite. The most common studies have described the zinc oxide phases in the form of zincite [54,55] and various sulfide and sulfate phases of lead and zinc [29].

Challacolloite was found for the first time in the dust of non-ferrous metallurgy. This mineral has not been described so far in dusts from non-ferrous metallurgy. Its natural occurrence is known in materials from volcanic eruptions and its occurrence has been found in a silver mine in Chile [56]. Synthetic challacolloite crystals are used in the production of lasers [57]. It is soluble in water, so it can easily be released into the environment.

According to Mössbauer spectra, the main iron bearing phases in steelmaking dust and sinter dust are hematite and magnetite. In scale dust an inverse spinel magnetite phase, hematite as well as wüstite were present and in dedusting dust—franklinite, magnetite, and jacobsite. Mössbauer spectra of the iron-bearing sludge dusts indicate presence of wüstite, metallic iron and less amount of hematite and magnetite, but also Fe^{3+} in amorphous matrix was detected.

Studies have shown that the magnetic susceptibility of a sample was determined not only by the elements present in significant amounts, but also by the elements present in trace amounts.

It has been proven that the samples, in which the presence of magnetite and other iron-bearing minerals is confirmed with XRD analysis and Mössbauer spectroscopy, are not always characterized by the highest values of magnetic susceptibility. The reason is that these analyses are qualitative analyses, but in case of magnetic susceptibility the quantitative content of magnetic minerals in the sample is responsible for its values.

Supplementary Materials: The following are available online at https://www.mdpi.com/2075-163X/11/2/216/s1, Table S1: Mössbauer spectroscopy parameter data of Fe-bearing dust minerals in samples from metallurgy.

Author Contributions: Conceptualization, M.J. and M.R.; methodology, M.J.; M.R.; M.W.; and M.K.-G.; validation, E.T. and T.K.; formal analysis, E.T. and T.K; investigation, M.J.; M.R.; M.W.; and M.K.-G.; resources, M.R.; M.J.; data curation, M.R.; M.J.; writing—original draft preparation, M.R.; M.J.; M.W.; and M.K.-G.; writing—review and editing M.R.; M.J.; M.W.; and M.K.-G.; visualization, D.S.-D.; supervision, M.R.; project administration, M.R. and M.J.; funding acquisition, M.R. All authors have read and agreed to the published version of the manuscript.

Funding: This research was funded by National Science Centre of Poland on the basis of the decision number DEC-2013/09/B/ST10/02227.

Data Availability Statement: The data presented in this study are available on request from the corresponding author.

Acknowledgments: This study was supported by National Science Center (NCN) on the basis of the decision number DEC-2013/09/B/ST10/02227 entitled "Magnetic and mineralogical identification of technogenic manganese and iron (hydro)oxides in industrial dusts and soils of Upper Silesia". We thank the Reviewers for their constructive comments that have improved the quality of the manuscript.

Conflicts of Interest: The authors declare no conflict of interest. The funders had no role in the design of the study; in the collection, analyses, or interpretation of data; in the writing of the manuscript, or in the decision to publish the results.

References

1. Jabłońska, M.; Janeczek, J. Identification of industrial point sources of airborne dust particles in an urban environment by a combined mineralogical and meteorological analyses: A case study from the Upper Silesian conurbation, Poland. *Atmos. Pollut. Res.* **2019**, *10*, 980–988. [CrossRef]
2. Kukier, U.; Ishak, C.F.; Sumner, M.E.; Miller, W.P. Composition and element solubility of magnetic and non-magnetic fly ash fractions. *Environ. Pollut.* **2003**, *123*, 255–266. [CrossRef]
3. Gupta, S.; Dubikova, M.; French, D.; Sahajwalla, V. Characterization of the origin and distribution of the minerals and phases in metallurgical cokes. *Energy Fuel* **2007**, *21*, 303–313. [CrossRef]
4. Magiera, T.; Jabłońska, M.; Strzyszcz, Z.; Rachwał, M. Morphological and mineralogical forms of technogenic magnetic particles in industrial dusts. *Atmos. Environ.* **2011**, *45*, 4281–4290. [CrossRef]
5. Magiera, T.; Gołuchowska, B.; Jabłońska, M. Technogenic magnetic particles in alkaline dusts from power and cement plants. *Water Air Soil Pollut.* **2013**, *224*, 1389. [CrossRef]
6. Thompson, R.; Oldfield, F. *Environmental Magnetism*; Allen and Unwin: London, UK, 1986; pp. 1–227.
7. Catinon, M.; Ayrault, S.; Boudouma, O.; Bordier, L.; Agnello, G.; Reynaud, S.; Tissut, M. Isolation of technogenic magnetic particles. *Sci. Total Environ.* **2014**, *475*, 39–47. [CrossRef]
8. Lu, S.; Yu, X.; Chen, Y. Magnetic properties, microstructure and mineralogical phases of technogenic magnetic particles (TMPs) in urban soils: Their source identification and environmental implications. *Sci. Total Environ.* **2016**, *543*, 239–247. [CrossRef]
9. Cornel, R.M.; Schwertmann, U. *The Iron Oxides. Structure, Properties, Reactions and Uses*; VCH: New York, NY, USA, 1996.
10. Zboril, R.; Mashlan, M.; Petridis, D. Iron(III) oxides from thermal processes synthesis, structural and magnetic properties, mössbauer spectroscopy characterization, and applications. *Chem. Mater.* **2002**, *14*, 969–982. [CrossRef]
11. Bhattacharjee, H.; Mandal, R.M.; Kusz, J.; Hofmeister, W. Microstructural and magnetic characterization of fly ash from Kolaghat Thermal Power Plant in West Bengal, India. *J. Magn. Magn. Mater.* **2011**, *323*, 3007–3012. [CrossRef]
12. Brown, P.; Jonesa, T.; BéruBé, K. The internal microstructure and fibrous mineralogy of fly ash from coal-burning power stations. *Environ. Pollut.* **2011**, *159*, 3324–3333. [CrossRef]
13. Jayaranjan, M.L.D.; van Hullebusch, E.D.; Annachhatre, A.P. Reuse options for coal fired power plant bottom ash and fly ash. *Rev. Environ. Sci. Biotechnol.* **2014**, *13*, 467–486. [CrossRef]
14. Petrovský, E.; Zboril, R.; Grygar, T.M.; Kotlik, B.; Novak, J.; Kapička, A.; Grison, H. Magnetic particles in atmospheric particulate matter collected at site with different level of air pollution. *Stud. Geophys. Geod.* **2013**, *57*, 755–770. [CrossRef]
15. Uzarowicz, Ł.; Zagórski, Z. Mineralogy and chemical composition of technogenic soils (Technosols) developed from fly ash and bottom ash from selected thermal power stations in Poland. *Soil Sci. Ann.* **2015**, *66*, 82–91. [CrossRef]
16. Kicińska, A. Chemical and mineral composition of fly ashes from home furnaces, and health and environmental risk related to their presence in the environment. *Chemosphere* **2019**, *215*, 574–585. [CrossRef] [PubMed]
17. Smołka-Danielowska, D.; Kądziołka-Gaweł, M.; Krzykawski, T. Chemical and mineral composition of furnace slags produced in the combustion process of hard coal. *Int. J. Environ. Sci. Technol.* **2019**, *16*, 5387–5396. [CrossRef]

18. Goodarzi, F. Characteristics and composition of fly ash from Canadian coal-fired power plants. *Fuel* **2006**, *85*, 1418–1427. [CrossRef]
19. Konieczyński, J.; Stec, K. The occurrence of selected trace elements in grain fractions of dust emitted from power, coke and cement plants. *Arch. Environ. Prot.* **2009**, *35*, 3–21.
20. Konieczyński, J.; Zajusz-Zubek, E. Distribution of selected trace elements in dust containment and flue gas desulphurisation products from coal-fired power plants. *Arch. Environ. Prot.* **2011**, *37*, 3–14.
21. Silva, L.F.O.; Ward, C.R.; Hower, J.C.; Izquierdo, M.; Waanders, F.; Oliveira, M.L.S.; Li, Z.; Hatch, R.S.; Querol, X. Mineralogy and Leaching Characteristics of Coal Ash from a Major Brazilian Power Plant. *Coal Combust. Gasif. Prod.* **2010**, *2*, 51–65. [CrossRef]
22. Gargiulo, J.D.; Chaparro, M.A. Particulate matter pollution from a small coke-burning factory: Soil magnetic screening and its relation with a simple atmospheric dispersion model. *Stud. Geophys. Geod.* **2016**, *60*, 316–331. [CrossRef]
23. Gołuchowska, B.; Strzyszcz, Z.; Kusza, G. Magnetic susceptibility and heavy metal content in dust from the lime plant and the cement plant in Opole Voivodeship. *Arch. Environ. Prot.* **2012**, *38*, 7–80. [CrossRef]
24. Paoli, L.; Winkler, A.; Guttová, A.; Sagnotti, L.; Grassi, A.; Lackovičová, A.; Senko, D.; Loppi, S. Magnetic properties and element concentrations in lichens exposed to airborne pollutants released during cement production. Environ. *Sci. Pollut. Res.* **2017**, *24*, 12063–12080. [CrossRef]
25. Rachwał, M.; Magiera, T.; Wawer, M. Coke industry and steel metallurgy as the source of soil contamination by technogenic magnetic particles, heavy metals and polycyclic aromatic hydrocarbons. *Chemosphere* **2015**, *138*, 863–873. [CrossRef] [PubMed]
26. Szumiata, T.; Rachwał, M.; Magiera, T.; Brzózka, K.; Gzik-Szumiata, M.; Gawroński, M.; Górka, B.; Kyzioł-Komisińska, J. Iron-containing phases in metallurgical and coke dust as well as in bog iron ore. *Nukleonika* **2017**, *62*, 187–195. [CrossRef]
27. Czaplicka, M.; Buzek, Ł. Lead speciation in the dusts emitted from non-ferrous metallurgy processes. *Water Air Soil Pollut.* **2011**, *218*, 157–163. [CrossRef] [PubMed]
28. Hleis, D.; Fernández-Olmo, I.; Ledoux, F.; Kfoury, A.; Courcot, L.; Desmonts, T.; Courcot, D. Chemical profile identification of fugitive and confined particle emissions from an integrated iron and steelmaking plant. *J. Hazard. Mater.* **2013**, *250*, 246–255. [CrossRef]
29. Adamczyk, Z.; Nowińska, K. Environmental mobility of trace elements present in dusts emitted from Zn–Pb metallurgical processes. *Environ. Earth Sci.* **2016**, *75*, 956. [CrossRef]
30. Omran, M.; Fabritius, T. Treatment of blast furnace sludge (BFS) using a microwave heating technique, Ironmak. *Steelmak* **2017**, *44*, 619–629. [CrossRef]
31. Lv, W.; Gan, M.; Fan, X.; Ji, Z.; Chen, X.; Yao, J.; Jiang, T. Recycling utilization of zinc-bearing metallurgical dust by reductive sintering: Reaction behavior of zinc oxide. *JOM* **2019**, *71*, 3173–3180. [CrossRef]
32. Stevens, J.G.; Khasanov, A.M.; Miller, J.W.; Pollak, H.; Li, Z. *Mössbauer Mineral Handbook*; Mössbauer Effect Data Center: Asheville, NC, USA, 2005; pp. 1–636.
33. Dyar, M.D. Precision and inter-laboratory reproducibility of measurements of the Mössbauer effect in minerals. *Am. Mineral.* **1984**, *69*, 1127–1144.
34. De Grave, E.; Van Alboom, A. Evaluation of Ferrous and Ferric Mössbauer Fractions. *Phys. Chem. Miner.* **1991**, *18*, 337–342. [CrossRef]
35. Eeckhout, S.G.; De Grave, E. Evaluation of ferrous and ferric Mössbauer fractions. Part II. *Phys. Chem. Miner.* **2003**, *30*, 142–146. [CrossRef]
36. Dyar, M.D. Optical and Mössbauer Spectroscopy of Iron in Micas. *Rev. Mineral. Geochem.* **2002**, *46*, 313–349. [CrossRef]
37. Rancourt, D.G.; McDonald, A.M.; Lalonde, A.E.; Ping, J.Y. Mössbauer absorber thickness for accurate site populations in Fe-bearing minerals. *Am. Mineral.* **1993**, *78*, 1–7.
38. Lecoanet, H.; Leveque, F.; Segura, S. Magnetic susceptibility in environmental applications: Comparison of field probes. *Phys. Earth Planet. Inter.* **1999**, *115*, 191–204. [CrossRef]
39. Hrouda, F. A technique for the measurement of thermal changes of magnetic susceptibility of weakly magnetic rocks by the CS-2 apparatus and KLY-2 Kappabridge. *Geophys. J. Int.* **1994**, *118*, 604–612. [CrossRef]
40. Anameric, B.; Komar, K.S. Direct iron smelting reduction processes, Mineral Processing and Extractive Metallurgy Review. *An Int. J.* **2008**, *30*, 1–51. [CrossRef]
41. Wang, G.C. *The Utilization of Slag in Civil Infrastructure Construction*; Nonferrous Metal Extraction and Nonferrous Slags; Elsevier Ltd.: Amsterdam, The Netherlands, 2016; pp. 35–61. [CrossRef]
42. Gheiratmand, T.; Hosseini, H.R.M.; Davami, P.; Gjoka, M.; Song, M. The effect of mechanical milling on the soft magnetic properties of amorphous FINEMET alloy. *J. Magn. Magn. Mater.* **2015**, *381*, 322–327. [CrossRef]
43. Kukurugya, F.; Vindt, T.; Havlík, T. Behavior of zinc, iron and calcium from electric arc furnace (EAF) dust in hydrometallurgical processing in sulfuric acid solutions: Thermodynamic and kinetic aspects. *Hydrometallurgy* **2015**, *154*, 20–32. [CrossRef]
44. Dyar, M.D.; Agresti, D.; Schaefer, M.; Grant, C.; Sklute, E. Mössbauer spectroscopy of earth and planetary materials. *Annu. Rev. Earth Planet. Sci.* **2006**, *34*, 83–125. [CrossRef]
45. Górka-Kostrubiec, B.; Werner, T.; Dytłow, S.; Szczepaniak-Wnuk, I.; Jeleńska, M.; Hanc-Kuczkowska, A. Detection of metallic iron in urban dust by using high-temperature measurements supplemented with microscopic observations and Mössbauer spectra. *J. Appl. Geophys.* **2019**, *166*, 89–102. [CrossRef]

46. Górka-Kostrubiec, B.; Magiera, T.; Dudzisz, K.; Dytłow, S.; Wawer, M.; Winkler, A. Integrated magnetic analyses for the discrimination of urban and industrial dusts. *Minerals* **2020**, *10*, 1056. [CrossRef]
47. Hagni, A.M.; Hagni, R.D.; Demars, C. Mineralogical characteristics of electric arc furnace dusts. *JOM* **1991**, *43*, 28–30. [CrossRef]
48. Jabłońska, M.; Smołka-Danielowska, D. Iron oxides particles in the air and fly ash, and their influence on the environment (preliminary studies). *PGI Spec. Pap.* **2008**, *24*, 93–98.
49. Haihan, C.; Laskin, A.; Baltrusaitis, J.; Gorski, C.; Scherer, M.; Grassian, V. Coal fly ash as a source of iron in atmospheric dust. *Envirol. Sci. Technol.* **2012**, *46*, 211–212. [CrossRef]
50. Jelenska, M.; Hasso-Agopsowicz, A.; Kopcewicz, B. Thermally induced transformation of magnetic minerals in soil based on rock magnetic study and Mossbauer analysis. *Phys. Earth Planet. Inter.* **2010**, *179*, 164–177. [CrossRef]
51. Oliweira, M.; Waanders, F.; Silva, L.; Jasper, A.; Sampaio, C.; McHabe, D.; Hatch, R.; Hower, J. A multi analytical approach to understand chemistry of Fe-minerals in fees coal and ashes. *Coal Combust. Gasif. Prod.* **2011**, *3*, 51–62. [CrossRef]
52. Fiałkiewicz-Kozieł, B.; Łokas, E.; Gałka, M.; Kołaczek, P.; De Vleeschouwer, F.; Le Roux, G.; Śmieja-Król, B. Influence of transboundary transport of trace elements on mountain peat geochemistry (Sudetes, Central Europe). *Quat. Sci. Rev.* **2020**, *230*, 106162. [CrossRef]
53. Hansson, R.; Hayes, P.C.; Jak, E. Phase equilibria in the ZnO-rich area of the Fe-Zn-O system in air, Scand. *J. Metall.* **2004**, *33*, 294–304. [CrossRef]
54. Papp, I.; Koleszar, P.; Kozak, M. Chemical composition and zinc leaching test of dust from electric arc furnace emissions from the Steelwork of Ózd, Hungary. *Acta GGM Debrecina Geol. Geomorphol. Phys. Geogr. Series Debr.* **2010**, *4–5*, 7–11.
55. Schlüter, J.; Pohl, D.; Britvin, S. The new mineral challacolloite, KPb2Cl5, the natural occurrence of a technically known laser material. *Neues Jahrb. Mineral. Abh.* **2005**, *182*, 95–101. [CrossRef]
56. Isaenko, L.I.; Dragomir, A.; McInerney, J.G.; Nikogosyan, D.N. Anisotropy of two-photon absorption in BBO at 264 nm. *Opt. Commun.* **2001**, *198*, 433–438. [CrossRef]
57. Fiałkiewicz-Kozieł, B.; De Vleeschouwer, F.; Mattielli, N.; Fagel, N.; Palowski, B.; Pazdur, A.; Smieja-Król, B. Record of Anthropocene pollution sources of lead in disturbed peatlands from Southern Poland. *Atmos. Environ.* **2018**, *179*, 61–68. [CrossRef]